

Image Profile (IMPRO) Fitting of Massive Protostars. I. Method Development and Test Cases of Cepheus A and G35.20-0.74N

YAO-LUN YANG,¹ JONATHAN C. TAN,^{2,3} RUBÉN FEDRIANI,⁴ AND YICHEN ZHANG⁵

¹*Star and Planet Formation Laboratory, RIKEN Pioneering Research Institute, Wako-shi, Saitama, 351-0198, Japan*

²*Department of Space, Earth & Environment, Chalmers University of Technology, 412 93 Gothenburg, Sweden*

³*Department of Astronomy, University of Virginia, Charlottesville, Virginia 22904, USA*

⁴*Instituto de Astrofísica de Andalucía, CSIC, Glorieta de la Astronomía s/n, E-18008 Granada, Spain*

⁵*Department of Astronomy, Shanghai Jiao Tong University, 800 Dongchuan Rd., Minhang, Shanghai 200240, People's Republic of China*

ABSTRACT

Massive stars play a critical role in the evolution of galaxies, but their formation remains poorly understood. One challenge is accurate measurement of the physical properties of massive protostars, such as current stellar mass, envelope mass, outflow cavity properties, and system orientation. Spectral energy distribution (SED) fitting is widely-used to test models against observations. The far-infrared SED traces cold dust in envelopes, while the near- and mid-infrared (MIR) probes emission from outflow cavities and/or the inner envelope. However, SED fitting has degeneracy limiting its ability to yield accurate measurements of protostellar properties. Here, we develop image profile (IMPRO) fitting as a method to improve the characterization of protostars. We utilize brightness distributions from multi-wavelength MIR images of massive protostars taken by SOFIA/FORCAST as part of the SOFIA Massive Star Formation (SOMA) survey to constrain protostellar properties via comparison to a grid of radiative transfer models. We develop a fitting pipeline to extract information along the outflow axis, which is then combined with the SED fitting to yield improved constraints on protostellar properties. We apply the IMPRO fitting method on the nearby massive protostar Cepheus A, finding that its properties become more tightly constrained compared to SED fitting, especially in the inclination of the source. However, for the more distant G35.20-0.74N, we find that the spatial resolution of SOFIA/FORCAST limits the utility of this combined fitting pipeline. However, higher resolution MIR observations, e.g., with JWST, are expected to greatly expand the applicability of this fitting technique to protostars across the Galaxy.

1. INTRODUCTION

Massive stars (i.e., with mass $m_* > 8 M_\odot$) play important roles in shaping the evolution of galaxies by their intense radiation, powerful winds, and supernovae, and enriching nucleosynthetic yields (e.g., Beuther et al. 2007; Tan et al. 2014). Constraining the formation processes of massive stars is a key step toward understanding the impact of massive stars on galaxy evolution. Furthermore, the radiative and mechanical feedback generated by massive stars also affects nearby molecular gas and the birth of lower mass stars. Several theories of massive star formation have been proposed, including the Turbulent Core Accretion (TCA) model (McKee & Tan 2003) and Competitive Accretion model (Bonnell et al. 2001). These models predict different signatures

testable by observations. For example, the turbulent core model expects a massive prestellar core supported by turbulence and/or magnetic fields, which then monolithically collapses due to gravity, resulting in a structure similar to low-mass protostellar cores, i.e., with a central disk and quasi-symmetric bipolar outflows. Competitive accretion predicts that massive star formation occurs in a protocluster, whose global potential controls the accretion flow to the massive protostar, which is more chaotic and disordered on small scales. To test these models, it is crucial to obtain improved observational constraints on the fundamental properties of massive protostars.

Direct observations of massive protostars have been challenging due to their embedded nature. While the extinction is much less at sub-mm and radio wavelengths, continuum observations in this regime mainly probe cold dust in the outer envelope or the midplane of the disk (Beltrán & de Wit 2016; Miotello et al. 2023). To better constrain protostellar properties, especially those re-

lated to the full bolometric luminosity, requires a more complete multi-wavelength approach that utilizes the radiative transfer of MIR emission through the protostellar core.

Zhang & Tan (2018) (hereafter ZT18) present a grid of radiative transfer simulations based on the TCA model. This model includes a protostellar envelope, an accretion disk, a disk wind powered bipolar outflow, and a central protostar (Zhang & Tan 2011; Zhang et al. 2013a, 2014). The ZT18 model grid is spanned by five parameters: initial core mass (M_c); the mean mass surface density of the surrounding clump (Σ_{cl}); the current protostellar mass (m_*); the viewing angle, defined as the angle between line of sight to the near-facing outflow axis (θ_{view}); and the equivalent V-band magnitude of foreground extinction (A_V). The first three parameters describe the physical models along protostellar evolutionary tracks, i.e., a separate track following an increasing m_* for various combinations of M_c and Σ_{cl} that describe initial core properties. The last two parameters aim to capture observational effects due to source orientation and foreground extinction. Use of the ZT18 grid has so far been limited to global SEDs, which are then fitted to observational data (e.g., De Buizer et al. 2017; Liu et al. 2019, 2020). In addition, Fedriani et al. (2023a) implemented ZT18 SED fitting via a python package, `sedcreator`¹. Telkamp et al. (2025) have developed methods to identify and fit SEDs of multiple sources in crowded regions.

However, while the SED fitting is a simple method to estimate the protostellar properties, the observed SED may not uniquely constrain model parameters. For example, in the “good” models returned by SED fitting, i.e., with acceptable values of the reduced χ^2 values, there can be large ranges of model grid parameters (see, e.g., Zhang & Tan 2018; Fedriani et al. 2023a). Spatial brightness distributions provide independent constraints that can break such degeneracies and thus reduce the uncertainties in derived protostellar properties. Zhang & Tan (2011); Zhang et al. (2013a, 2014) demonstrated distinct brightness profiles along the outflow direction at different viewing angles, suggesting that this radial brightness profile could provide an independent constraint for fitting the parameters in the ZT18 grid. Zhang et al. (2013b) presented an example of fitting brightness profiles along a massive protostellar outflow. Using a different modeling approach, Frost et al. (2019) showed that multi-scale observations, where the highest resolution observations probe down to the disk scale, can more robustly constrain models to reproduce the

observed SED and the brightness distributions at different scales. A larger survey modeled with this method allows further exploration of the disk evolution in massive protostars (Frost et al. 2021a,b).

Here, we present a modeling method for massive protostars, fitting both the SED and the radial brightness profile along the outflow axis with the ZT18 grid. Section 2 describes the fitting method and how we combine the SED and the radial profiles. Section 3 presents two case studies of massive protostars, Cepheus A and G35.20–0.74N, which we fit by this method. We also discuss the performance of our new fitting method compared with SED-only fitting. Finally, Section 4 summarizes the conclusions of our study.

2. METHOD

Uncertainty in viewing angle is one of the major sources of degeneracy for the results of fitting SED models to observed protostars. As a result of low-density outflow cavities, the SED of a dense envelope viewed from the outflow direction can appear similar to the SED of a less dense envelope viewed closer to the mid-plane. This issue leads to degeneracy between the viewing angle and the core properties in SED models. While ZT18 presents a self-consistent SED model grid of massive protostars, the degeneracy due to the viewing angle inevitably hinders an accurate characterization of a protostar. Outflow morphology provides a way to break this degeneracy. A protostellar envelope with an inclined outflow cavity would have uneven brightness between the two outflow lobes. The asymmetric brightness becomes more obvious at shorter wavelengths, where extinction is notably higher toward the red-shifted, far-facing outflow. Thus, the asymmetry in the image may provide unique constraints on the inclination and help to break degeneracies in SED model fitting.

We develop a method to better constrain the properties of protostellar cores by fitting for the brightness profile along the outflow together with the SED modeling developed by ZT18. Figure 1 illustrates steps in this method. To limit the number of degrees of freedom, we extract the brightness profile from a strip along the outflow axis. The strip has a default width of $20''$ (see the discussion in Section 3.1.2), whereas the beam size of SOFIA/FORCAST at $37\ \mu\text{m}$ is about $3''.5$. Averaging the brightness along the width of the strip, we can extract a 1D brightness profile from observations. To constrain the protostellar model, we perform the same extraction in all models in the ZT18 grid. In ZT18, only the synthetic SEDs are presented. However, the model images are also produced as part of the radiative transfer calculations. Example model images were presented in

¹ <https://sedcreator.readthedocs.io/en/latest/>

Zhang et al. (2014). The model grid assumes a distance of 1 kpc, so we first calculate the distance-corrected angular size of the model image and then extract the 1D profile with a strip of the same width. For partially included pixels, the calculations of the average brightness take the fractional brightness according to the included area. In this section, we use the SOFIA/FORCAST 37 μm image of Cepheus A as an example to demonstrate this 1D profile fitting pipeline. The full fitting pipeline includes the images at 19.7, 31.5, and 37.0 μm (see Section 3.1.2). Figure 1c shows the 1D profile from the 37 μm image of Cepheus A and a protostellar model.

Being located at large distances of $\gtrsim 1$ kpc, massive protostars often have significant foreground extinction, which needs to be accounted for when comparing observed systems with theoretical models. The ZT18 SED model grid considers the extinction (A_V) separately by minimizing the χ^2_{SED} in each model SED with A_V ranging from 0 to 1000 (Fedriani et al. 2023a), but the model images do not include the effect of A_V . Furthermore, the model only includes the protostellar core, whereas the core often resides within a clump, which emits significant “background” emission. Thus, to realistically compare the modeled 1D profiles (I_{model}) with the observed 1D profile (I_{obs}), we need to consider the effects of such foreground extinction and background emission.

For each model, we consider the emission in observational data from outside of the model core radius (Equation 1; see also ZT18) as the background emission. The background emission is determined at the core radius ($\pm R_c$ in the 1D profile) and linearly interpolated along the strip. In the TCA model, the core radius is given by

$$\frac{R_c}{\text{pc}} = 5.7 \times 10^{-2} \left(\frac{M_c}{60 M_\odot} \right) \left(\frac{\Sigma_{\text{cl}}}{\text{g cm}^{-2}} \right)^{-0.5}. \quad (1)$$

The estimated background emission from observations is the background emission with foreground extinction. To compare the model against the observations, we apply the foreground extinction to the modeled intensity (I_{model}) and include the estimated background emission (I_{bkg}), resulting in a synthetic 1D brightness profile (I_{syn}). The relations between these variables are given by

$$\begin{aligned} I_{\text{syn}} &= I_{\text{model}} f_{A_V} + I_{\text{bkg}}; \\ f_{A_V} &= 10^{-0.4 A_V (\kappa_\lambda / \kappa_V)}, \end{aligned} \quad (2)$$

where the κ_V is the dust opacity at V-band (0.55 μm). The extinction relation follows the prescription in ZT18, which uses the extinction law in Kim et al. (1994).

We consider A_V as an independent parameter and sample it in a logarithmic scale from 1 to 1000 mag with

100 points, in addition to $A_V=0$. Thus, there are five parameters in the protostellar models, core mass (M_c), mass surface density (Σ_{cl}), protostellar mass (m_*), viewing angle of line of sight to outflow axis (θ_{view}), and foreground extinction (A_V). ZT18 sampled the first three parameters with 432 models to construct the grid of SED models. The viewing angle was sampled linearly in $\cos \theta_{\text{view}}$ with 20 points from 0° to 90° . In total, the model grid has 8640 models without considering A_V . To find the best-fitting models, we derive the χ^2 of each model by comparing it with the 1D profile extracted from observations. To avoid over-sampling the spatial resolution, we then resampled the 1D profiles of I_{obs} and I_{syn} onto a coarse grid with each element separated by the spatial resolution of the observations, resulting in $I_{\text{obs,bin}}$ and $I_{\text{syn,bin}}$. The adopted beam size is $3''.5$, $3''$, $2''.5$, and $2''.5$ for 37.0, 31.5, 19.7, and 7.7 μm images, respectively. Furthermore, we only consider the brightness within the model R_c . For each model, we calculate the reduced χ^2_{IMPRO} as

$$\chi^2_{\text{IMPRO}} = \frac{1}{n_{\text{bin}} - 1} \sum \left(\frac{(I_{\text{obs,bin}} - I_{\text{syn,bin}})^2}{\sigma^2} \right), \text{ where} \quad (3)$$

$$\sigma = \sqrt{(0.1 I_{\text{obs,bin}})^2 + (0.1 I_{\text{bkg,bin}})^2},$$

assuming a 10% uncertainty on I_{obs} and I_{bkg} , consistent with the assumption adopted in the SOMA papers (e.g., De Buizer et al. 2017). The n_{bin} is the number of resampled data points along the 1D profile within R_c .

In addition to χ^2_{IMPRO} , we use the modeling pipeline in Fedriani et al. (2023a) to derive the χ^2_{SED} from the SED using the full set of parameters (Figure 1d). The original pipeline in ZT18 steps A_V from 0 to 100 mag for each combination of M_c , Σ_{cl} , m_* , θ_{view} and only reports the model with the minimum χ^2 . Fedriani et al. (2023a) revised the SED modeling pipeline, called **sedcreator**, to (1) find the best-fitting A_V from 0 to 1000 mag with a minimization algorithm for combination of M_c , Σ_{cl} , m_* , θ_{view} ; and (2) convolve the synthetic SED with photometric filters before applying the effect of A_V , while the original ZT18 pipeline performs these two steps in the opposite order, resulting in small but noticeable differences (Fedriani et al. 2023a). While **sedcreator** allows us to treat A_V as an independent parameter, consistent with the treatment in the fitting of the 1D radial profiles, these two pipelines differ in their sampling of the same range of A_V . The **sedcreator** algorithm finds an A_V from 0 to 1000 mag that best fits the SED, whereas the imaging fitting pipeline uses a logarithmic grid of 100 points from 1 to 1000 mag, as well as considering $A_V=0$. Thus, we modified **sedcreator** to perform a grid search using the same A_V grid of the imaging fitting pipeline. Comparing with the default fitting results

of the `sedcreator`, the χ^2_{SED} of the best-fitting model for each combination of M_c , Σ_{cl} , m_* , θ_{view} only differs $\lesssim 6\%$ due to the slight mismatch of the A_V grid. In the SED fitting, we treat the mid-infrared fluxes at $<10\ \mu\text{m}$ (mostly the Spitzer/IRAC photometry) as upper limit because PAH emission, which is not considered in the modeling, can contaminate the photometric fluxes. To assess the goodness of fit, we weight the 1D profile and the SED equally by averaging the χ^2_{IMPRO} and χ^2_{SED} to have a combined $\chi^2_{\text{SED+IMPRO}}$. For a first exploration, we consider the models with their $\chi^2_{\text{SED+IMPRO}}$ no greater than the minimum $\chi^2_{\text{SED+IMPRO}} + 2$ as the “good” models, which is similar to the method used for selecting good models via SED fitting by (Fedriani et al. 2023a).

3. RESULTS AND ANALYSIS

We applied the 1D profile fitting pipeline to two well-studied sources in the SOMA survey, Cepheus A (hereafter Cep A) and G35.20–0.74N (hereafter G35.2N) (De Buizer et al. 2017). Cep A is one of the closest massive protostars ($d \sim 700\text{ pc}$) and has well-characterized outflows, so that the asymmetric brightness distribution due to the outflows is well-resolved by SOFIA-FORCAST. G35.2N, on the other hand, is further away at 2.2 kpc (Zhang et al. 2009). Zhang et al. (2013b) fitted the 1D brightness profile along the outflow direction using a model based on an earlier version of the ZT18 model grid but with extended outflow and clump environment structures.

3.1. Cepheus A

Located at 700 pc (Moscadelli et al. 2009), Cep A is the second closest massive star-forming region (with Orion being the closest at 400 pc). Thus, photometric surveys, such as SOMA, have a better physical resolution ($\sim 2000\text{ au}$) at Cep A to probe the asymmetric warm dust continuum due to outflows. In the development of the fitting pipeline, we thus used Cep A to optimize the choice of the strip width and the combination of photometric bands, which are discussed in the following sections.

3.1.1. The Outflows and Protostars in Cep A

Cep A has a main bipolar outflow axis oriented in the east-west directions, with a full extent of $\sim 1\text{ pc}$, first detected by Rodriguez et al. (1980). While the large-scale outflows orient in the E-W direction, the compact emission near Cep A traces outflows in the NE-SW direction. Together with the bow shocks traced by H_2 , Cunningham et al. (2009) infer a pulsed, precessing jet in Cep A. The CO $J = 3 \rightarrow 2$ emission traces this outflow

at $|v - v_{\text{source}}| < \sim 20\text{ km s}^{-1}$, where $v_{\text{source}} = -11.15\text{ km s}^{-1}$. At high velocity, $20 < |v - v_{\text{source}}| < 70\text{ km s}^{-1}$, the CO emission shows a compact bipolar outflow morphology with a position angle (PA) of about 40° – 60° with a length of $\sim 0.4\text{ pc}$. The compact outflow also appears in $\text{HCO}^+ J = 1 \rightarrow 0$ emission, as well as in thermal radio emission. The HCO^+ outflows have velocities up to $\sim 50\text{ km s}^{-1}$, extending $\sim 1'$ ($\sim 0.2\text{ pc}$) with a PA of 55° – 60° (Gómez et al. 1999). The MIR emission focused in this study traces compact NE-SW outflows.

Hughes & Wouterloot (1984) identified a cluster of radio sources at the center of the bipolar outflows, where HW2 is the strongest source with a flux density of $15.8 \pm 0.3\text{ mJy}$ at 14.9 GHz (Garay et al. 1996). High resolution and multi-frequency observations suggest HW2 as a biconical thermal jet with a proper motion of $\sim 500\text{ km s}^{-1}$ (Curiel et al. 2006). Among the radio sources, only HW2 and HW3c exhibit strong continuum at $870\ \mu\text{m}$, suggesting that HW2 is the most luminous protostar, followed by HW3c (Brogan et al. 2007). The total luminosity of Cep A has been previously estimated to be $2.5 \times 10^4 L_\odot$ (Evans et al. 1981). The SOMA SED fitting result for Cep A, updated in the latest SED fitting version by Telkamp et al. (2025), derives an intrinsic bolometric luminosity of $L_{\text{bol}} = 4.9^{+2.8}_{-1.8} \times 10^4 L_\odot$ and an isotropic bolometric luminosity (based on the observed bolometric flux) of $L_{\text{bol,iso}} = 2.0^{+0.5}_{-0.4} \times 10^4 L_\odot$, with these uncertainties reflecting the dispersion in the “good” SED model fits.

Many studies consider HW2 as the driving source of the complex outflows in Cep A. In our analysis, we will use the radio position of this source to define the location of the protostar (see De Buizer et al. 2017; Rosero et al. 2019). Positive values of offset are defined to be in the direction of the near-facing, blue-shifted outflow axis.

Variability is also known in Cep A from methanol maser monitoring observations (Sugiyama et al. 2008; Durjusz et al. 2022). The observed date of the SOFIA-FORCAST data used in this study, 2014 March 25, corresponds to an epoch of a minor variation in methanol maser emission. Thus, the interpretation of the fitting results may be affected by the variability, although our fitting method cannot distinguish the magnitude of the impact.

Observations of the $2.12\ \mu\text{m}$ H_2 trace several Herbig-Haro (HH) objects along the NE-SW outflows. To the west of HW2, HH 168 (also known as GGD 37; Gyulbudaghian et al. 1978; Reipurth & Raga 1999) is the brightest HH object in the complex (Hartigan et al. 1986, 2000; Green et al. 2011). The precessing jet inferred by Cunningham et al. (2009) also considers HW2 as the driving sources, which results in most of the HH

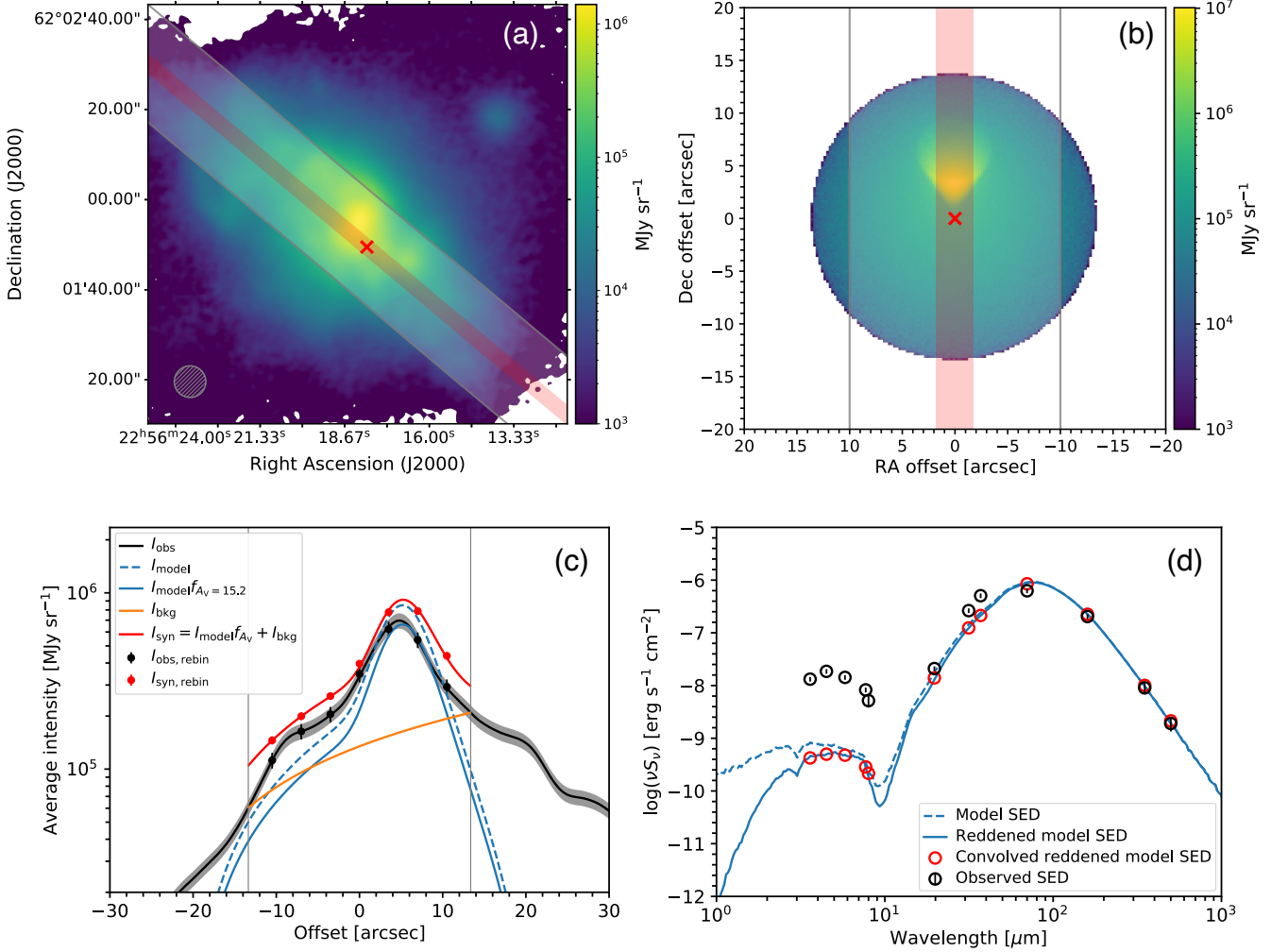


Figure 1. Illustrations of steps in the combined IMPRO + SED fitting pipeline. (a) The $37\ \mu\text{m}$ FORCAST image, as an example, overlaid with two strips of $3.5''$ and $20''$ width (red and white) along the outflow direction ($\text{PA}=50^\circ$). The beam size is shown at the bottom left, and the protostar is marked with a red “x” (defined from radio continuum emission). (b) The $37\ \mu\text{m}$ synthetic image overlaid with the same two strips of $3.5''$ and $20''$ width. The source is centered at the red “x” and the outflow axis is aligned N-S. (c) The extracted 1D brightness profiles along the strips. Each profile can be related using Equation 2. The χ^2 value is derived by comparing the rebinned observed profile (black circles) against the rebinned synthetic profile (red circles). Panels (c) and (d) show the best-fitting model considering both the 1D profile and the SED. The A_V adopted in this example is 15.2 mag. (d) The observed SED compared with the synthetic SED of the best-fitting model. The black and red circles show the fluxes at the wavelengths where photometry is available. The synthetic SED (red circles) is derived by reddening the SED convolved with photometric filters. The blue solid and dashed lines show the synthetic SED with and without extinction.

objects to the east and northeast, while the HW3c may be the driving source of HH 168.

Sanna et al. (2017) derived an outflow inclination (θ_{view}) of 26° by modeling a planar motion from observations of CH_3OH maser. Patel et al. (2005) derived a disk inclination of 62° from fitting a Keplerian motion to the CH_3CN emission, suggesting an outflow inclination (θ_{view}) of 28° if the outflow is perpendicular to the disk. They also derived a binding mass of $19 \pm 5\ M_\odot$ from the observed line width. However, Brogan et al. (2007) discovered distinct chemical differentiation along

the presumed disk major axis, suggesting the presence of multiple hot cores at a separation of $\sim 1''$ instead of a disk. Interestingly, Zapata et al. (2013) proposed that the precession at large scales may be due to the dynamical interactions between companions. The dust emission remains elongated at $0''.6$, supporting the existence of a disk, while multiple hot cores could exist in the vicinity of the dominant protostar (Torrelles et al. 2007). At $\sim 30\ \text{mas}$ ($\sim 20\ \text{au}$) resolution, Carrasco-González et al. (2021) found a highly collimated bipolar feature at 40 GHz that can be reproduced with a collimated jet along

with a wide-angle wind, which was also suggested by Torrelles et al. (2011). The abundant observational constraints on both the central protostar and the small-scale ($< 1'$) outflow make Cep A an ideal target to test the fitting of the radial brightness profiles.

3.1.2. IMPRO Fitting the Outflow Axis Intensity Profiles

Strip width - While Section 2 outlines the prescription of fitting the radial brightness profile, we need to first test the fitting setup, such as the strip width and the choice of photometric bands, to have the most robust fitting results. A good choice of the strip width would robustly constrain the viewing angle (θ_{view}). We tested three strip widths, $3''.5$, which is similar to the size of the SOFIA beam at $37\mu\text{m}$, $10''$, and $20''$. The width of the latter two strips is larger than the substructures seen in the outflows (Figure 1a). We define the “good” models as those with $\chi^2_{\text{min, IMPRO}} < \chi^2_{\text{IMPRO}} < \chi^2_{\text{min, IMPRO}} + 2$, to examine the performance of the fitting with different strip widths. This examination aims to determine the ideal strip width for fitting the 1D profiles, thus focusing only on the χ^2 calculated from the extracted 1D profile. The observed 1D profiles peak at $\sim 5''$ with a slight increase in the profile extracted with a wider strip (Figure 2). However, the peak of the synthetic 1D profiles changes significantly from $\sim 2''$ to $\sim 4''$ as the strip width increases. As a result, the difference of the peak positions between the observed and synthetic 1D profiles reduces when the strip width increases, hinting at a better fit. Figure 3 shows the distributions of all five model parameters among the good models for three different strip widths. The best-fitting values are determined by the mean from the good models, and the uncertainties are estimated from the mean value to the minimum and maximum values of the good models. The best-fitting model parameters span wide ranges of values in the fitting using a narrow strip. For example, the θ_{view} values span the entire possible range (0° – 90°) in the fittings with $3''.5$ and $10''$ wide strips, whereas the fitting with a $20''$ wide strip results in a narrow distribution of θ_{view} . The best-fitting θ_{view} distributions of all three fittings peak at a similar value, suggesting that they produce consistent results; however, the fitting with a $20''$ wide strip provides more diagnostic constraints. Thus, we define the strip width as $20''$ for the results shown in the following sections. More generally, the choice of strip width will depend on various source properties, especially distance, so it should be considered to be a user-defined parameter of the fitting procedure.

Photometric bands - The asymmetric brightness due to the orientation of outflow cavities would appear in the images at the wavelengths sensitive to warm dust

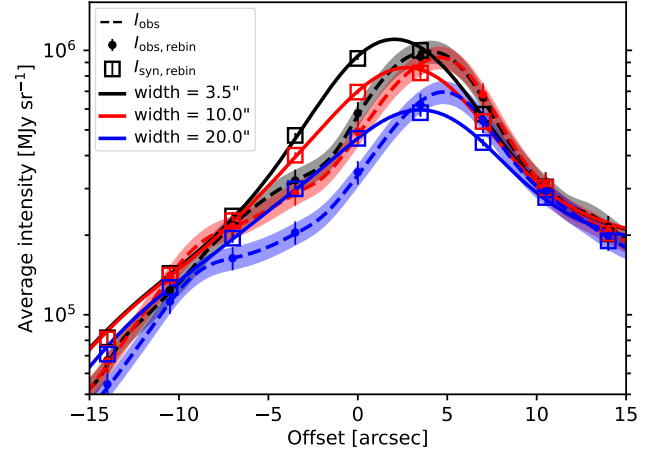


Figure 2. The 1D observed (dashed) and synthetic (solid) $37\mu\text{m}$ image intensity profiles derived with a strip widths of $3''.5$ (black), $10''$ (red), $20''$ (blue). The physical model has $M_c = 160 M_\odot$; $\Sigma_{\text{cl}} = 3.16 \text{ g cm}^{-2}$; $M_* = 64 M_\odot$; $\theta_{\text{view}} = 74^\circ$ and is the same for all three sets of profiles. The rebinmed observed and synthetic intensities are shown in filled circles and open squares, respectively.

emission and/or extinction. Therefore, we can leverage the multi-band images acquired by the SOMA survey at 19.7 , 31.5 , and $37.0\mu\text{m}$ to explore the benefits of a combined fitting of the 1D profiles in multi-band images. We exclude the $7.7\mu\text{m}$ image from the SOMA survey because of the possible contamination of the polycyclic aromatic hydrocarbon (PAH) emission. In the multi-band fitting pipeline, we first extracted the 1D observed and synthetic profiles in each band. We rebinned the 1D profiles to their corresponding resolutions, $2''.5$, $3''.0$, and $3''.5$ for 19.7 , 31.5 , and $37.0\mu\text{m}$, respectively. Then, we calculated a reduced χ^2_{1D} over three 1D profiles with equal weighting of each rebinned data point.

Simultaneous fitting of the 1D profiles from three FORCAST bands, 19.7 , 31.5 , and $37.0\mu\text{m}$, provides better diagnostic constraints on the protostellar model. Figure 4 shows the model parameters of the good models fitted with three choices of band combinations: $37.0\mu\text{m}$; $37.0\mu\text{m} + 31.5\mu\text{m}$; and $37.0\mu\text{m} + 31.5\mu\text{m} + 19.7\mu\text{m}$. The fittings constrain the model parameters within a relatively narrow range of values regardless of the choice of band combination, except that the A_V has a much smaller range in the three-band fitting. The fittings with only $37.0\mu\text{m}$ and $37.0\mu\text{m} + 31.5\mu\text{m}$ yield similar results, suggesting that the emission at these two bands comes from similar structures. By including the $19.7\mu\text{m}$ band, we have a better constraint on A_V by having a larger wavelength coverage. Consequently, the good models have a narrower range for each model parameter, especially A_V . There are also fewer good models in the

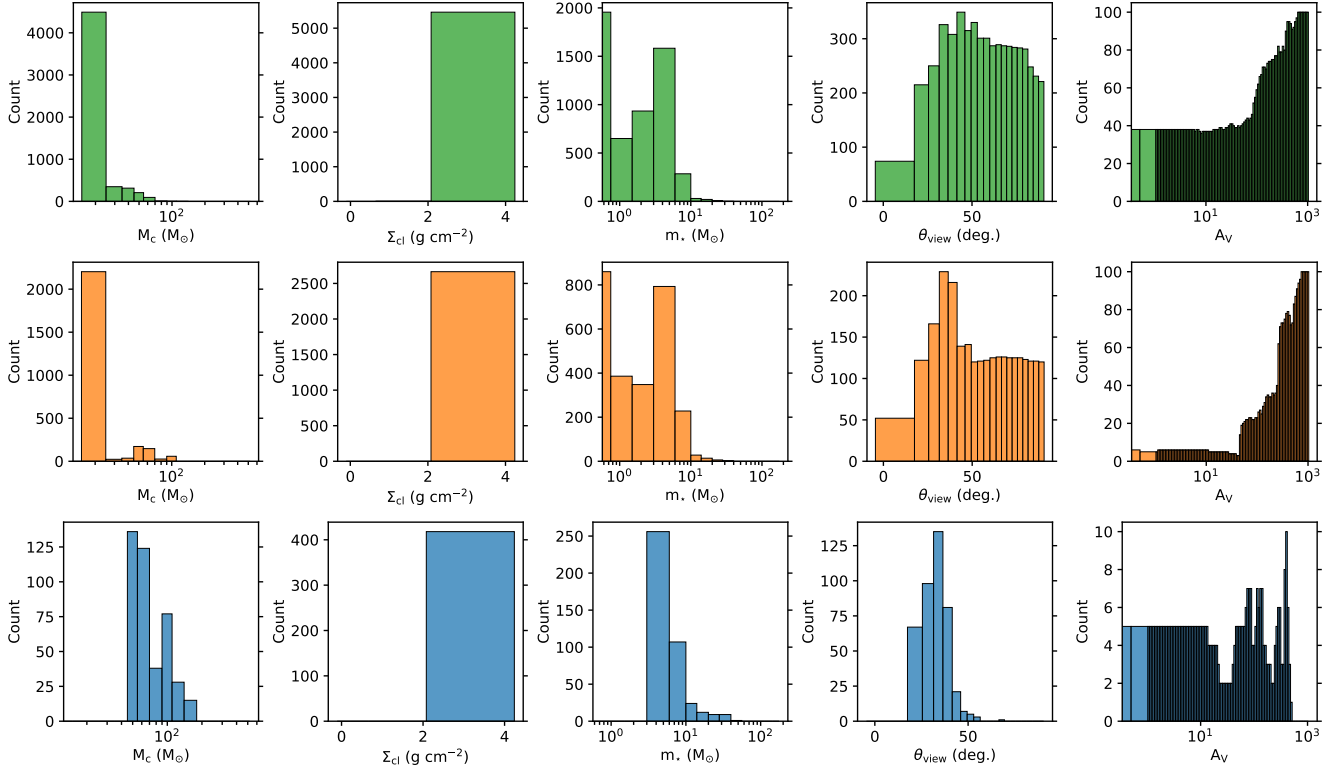


Figure 3. Distributions of the model parameters of the good 1D profile models ($\chi^2_{\min, \text{IMPRO}} < \chi^2_{\text{IMPRO}} < \chi^2_{\min, \text{IMPRO}} + 2$). The strip widths are $3.5''$, $10''$, and $20''$ from top to bottom. These fittings include only the $37 \mu\text{m}$ image.

fitting with all three bands, indicating a stronger constraint on model parameters. Thus, we simultaneously fit the 1D radial profiles of three FORCAST bands (19.7 , 31.5 , and $37.0 \mu\text{m}$) with a $20''$ strip to constrain the 1D profile.

3.1.3. Combined IMPRO and SED Fitting

As described in Section 2, the χ^2_{IMPRO} is combined with χ^2_{SED} to derive a combined χ^2 ($\chi^2_{\text{SED+IMPRO}}$) to assess the goodness of the IMPRO fitting of the 1D intensity profile along the outflow axis and the SED fitting. The distributions of the χ^2_{SED} and χ^2_{IMPRO} marginalized by model parameters demonstrate the distinctive constraining power of each method (Figures 5 and 6). When only fitting the SED, M_c and m_* are the most constrained compared to other parameters. The M_c and Σ_{cl} values appear negatively correlated. Both M_c and Σ_{cl} contribute to the total dust mass probed by the SED at far-infrared and sub-mm wavelengths, resulting in the degeneracy of these two parameters. However, the SED fitting yields robust constraints on M_c and m_* , effectively breaking the degeneracy between M_c and Σ_{cl} . The θ_{view} and A_V , on the other hand, remain poorly constrained via SED fitting. For any given Σ_{cl} , a wide range of θ_{view} produces similar quality of fits. For M_c and m_* , θ_{view} appears to be better characterized, al-

though still exhibiting significant degeneracy. The values of A_V show positive correlation with m_* , because the more evolved sources (higher m_*) would have more near-IR emission due to less material in the surrounding envelope, which requires a higher foreground A_V to produce the same near-IR fluxes. The χ^2_{SED} distribution of A_V and θ_{view} shows multiple strips of negative correlation. A source with a higher θ_{view} would have a redder SED, while A_V has a similar effect on the SED.

The distribution of χ^2_{IMPRO} exemplifies the constraining power of IMPRO fitting that is distinct from that resulting from SED fitting. The good models have a narrow range of θ_{view} in all distributions marginalized by θ_{view} . Particularly, the relation between m_* and θ_{view} is well characterized, whereas the SED fitting only puts a loose boundary on these parameters. The best-fitting parameters qualitatively agree with those derived from SED fitting. However, the parameters that produce the lowest χ^2 disagree. IMPRO fitting prefers a high Σ_{cl} , whereas SED fitting prefers a lower Σ_{cl} , although the χ^2_{SED} varies relatively less with Σ_{cl} compared to other parameters. With the inputs from only 19 – $37 \mu\text{m}$, IMPRO fitting has little information on the overall dust mass and the peak of the luminosity, which requires data at far-IR wavelengths.

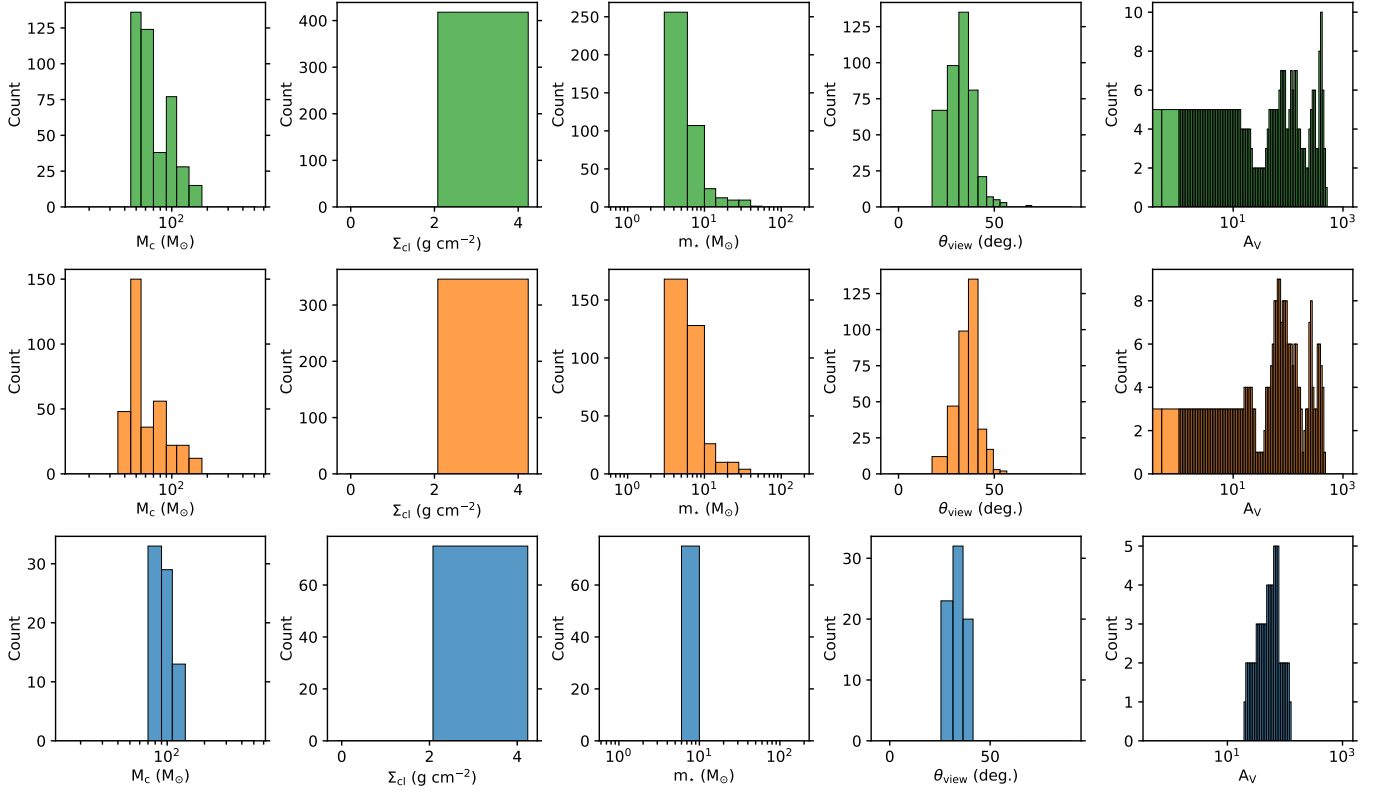


Figure 4. Distribution of the model parameters of the good 1D profile models ($\chi_{\min, \text{IMPRO}}^2 < \chi_{\text{IMPRO}}^2 < \chi_{\min, \text{IMPRO}}^2 + 2$) by fitting only $37 \mu\text{m}$, $37 \mu\text{m} + 31 \mu\text{m}$, and $37 \mu\text{m} + 31 \mu\text{m} + 19 \mu\text{m}$ images (from top to bottom) using a $20''$ strip width.

Figure 7 shows the marginalized $\chi_{\text{SED+IMPRO}}^2$ distribution of the combined IMPRO and SED fitting for Cep A. As described in Section 2, the $\chi_{\text{SED+IMPRO}}^2$ is the average of χ_{SED}^2 and χ_{IMPRO}^2 , giving them an equal weight. The distributions, therefore, present the characteristics of each fitting method discussed in the previous paragraphs. Most model parameters have local minima in these marginalized $\chi_{\text{SED+IMPRO}}^2$ distributions, while A_V has a shallower χ^2 minimum, which may be due to the weaker constraining power of the SED fitting. The minimum $\chi_{\text{SED+IMPRO}}^2$ is higher than either the minimum χ_{SED}^2 or the minimum χ_{IMPRO}^2 , suggesting that this fitting method, despite the improved constraints in A_V and θ_{view} , cannot fully capture the comprehensive properties of the massive protostellar cores. The minimum $\chi_{\text{SED+IMPRO}}^2$ is 6.58, also hinting at some limitations of the ZT18 model grid.

3.1.4. Best-fitting Parameters of Cep A

Figure 8 shows the distribution of the model parameters among the good models for the fitting using the SED-only, IMPRO-only, and SED+IMPRO. Similar to the discussion in Section 3.1.3, the SED fitting has relatively poor constraints on M_c , Σ_{cl} , θ_{view} , and A_V . The M_c of the good models ranges over $\sim 50 - 400\%$ of the mean value. The good models show a broad distribution

of Σ_{cl} , peaking at the 1.0 g cm^{-2} bin, while the distribution of M_c also has multiple peaks. Moreover, θ_{view} is hardly constrained, with a broad distribution ranging from 29° to $\sim 90^\circ$. The non-normal distribution of M_c suggests an irregularly shaped χ^2 space, possibly due to the ill-constrained θ_{view} . On the other hand, IMPRO fitting constrains θ_{view} within $\sim 5^\circ$ of the mean value. The fitted M_c and m_* have a similar mean value as that of the SED fitting with a single prominent peak. All the good models have the same Σ_{cl} and m_* , resulting in a single-binned histogram in the distribution. In this case, we take the uncertainty as the sampling interval of the model parameter. IMPRO fitting also constrains A_V with a narrow distribution. IMPRO fitting alone can reproduce the mean values of the model parameters found from SED fitting and yield Gaussian-like distributions, suggesting a more robust fitting result. Figure 8 (bottom) shows the model parameters estimated with the combined SED + IMPRO fitting. The mean values of model parameters are similar to those derived with IMPRO fitting, suggesting that the 1D intensity profiles have a stronger influence on the resulting $\chi_{\text{SED+IMPRO}}^2$.

Figure 9 shows the models with the lowest χ^2 fitted by the SED, IMPRO, and SED+IMPRO methods. As expected, the best-fitting model for the SED fitting re-

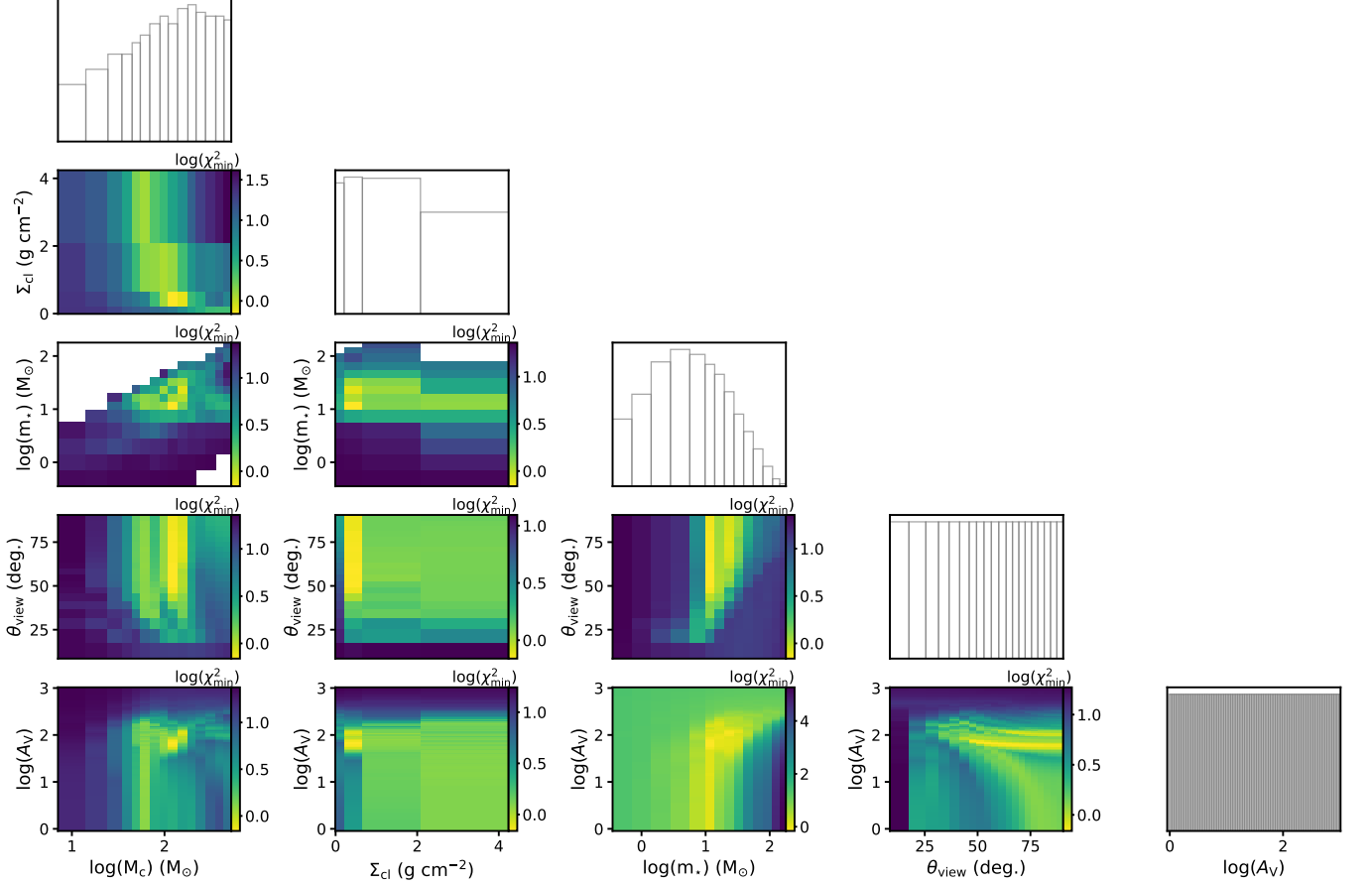


Figure 5. Distributions of the χ^2_{SED} marginalized by model parameters. Each panel shows the distribution of the lowest χ^2_{SED} at the given combination of model parameters. The histograms in gray illustrate the distribution of the sampled parameters and their spacings.

Table 1. The best-fitting model parameters of Cep A

Parameters	Fitting method		
	χ^2_{SED}	χ^2_{IMPRO}	$\chi^2_{\text{SED+IMPRO}}$
M_c (M_{\odot})	$87.0^{+393.0}_{-37.0}$	$94.7^{+25.3}_{-14.7}$	$95.7^{+24.3}_{-15.7}$
Σ_{cl} (g cm^{-2})	$1.4^{+1.8}_{-1.3}$	$3.2^{+1.1*}_{-1.1}$	$3.2^{+1.1*}_{-1.1}$
m_* (M_{\odot})	$14.2^{+33.8}_{-6.2}$	$8.0^{+4.0*}_{-2.0}$	$8.0^{+4.0*}_{-2.0}$
θ_{view} ($^{\circ}$)	$71.6^{+17.4}_{-49.6}$	$33.8^{+5.2}_{-4.8}$	$33.9^{+5.1}_{-4.9}$
A_V (mag)	$43.7^{+187.3}_{-43.7}$	$57.0^{+66.3}_{-36.9}$	$39.2^{+60.8}_{-28.4}$

NOTE: The uncertainties are taken from the full range of the distributions shown in Figure 8. The asterisk indicates that all the good models have the same value for the model parameter. The uncertainties are then taken as the size of the sampling interval at the best-fitting value.

produces the observed SED. The best-fitting SED model produces 1D profiles largely inconsistent with the observed profiles. The brightness in the SED model peaks at the source position, while the observed profiles have their brightness peak at an offset position. The 1D profiles from the SED model also underestimate the bright-

ness at positive offsets corresponding to the blue-shifted outflow cavity. On the other hand, the best IMPRO fitted model reproduces the observed 1D profiles except for the exact shape of the 1D profile at $19.7 \mu\text{m}$. The synthetic 1D profile at $19.7 \mu\text{m}$ has a smaller contrast between two outflow cavities compared to that shown in the observed profile. However, both profiles peak at a similar position. The best-fitting IMPRO model yields a worse SED model, which reproduces the far-infrared fluxes but underestimates the mid-infrared fluxes. The synthetic fluxes at $3\text{--}8 \mu\text{m}$ are much lower than that in the best-fitting SED model, although we treat the observed fluxes at these wavelengths as upper limits due to potential contamination from PAHs and transiently-heated small dust grains (see Fedriani et al. 2023a) so that the impact on the fitting is negligible. The best model in the combined fitting shows similar 1D profiles and SEDs as those of the best-fitting IMPRO model. Also, similar to the IMPRO fitting result, the $20\text{--}40 \mu\text{m}$ range of the SED is underestimated by the best-fitting model.

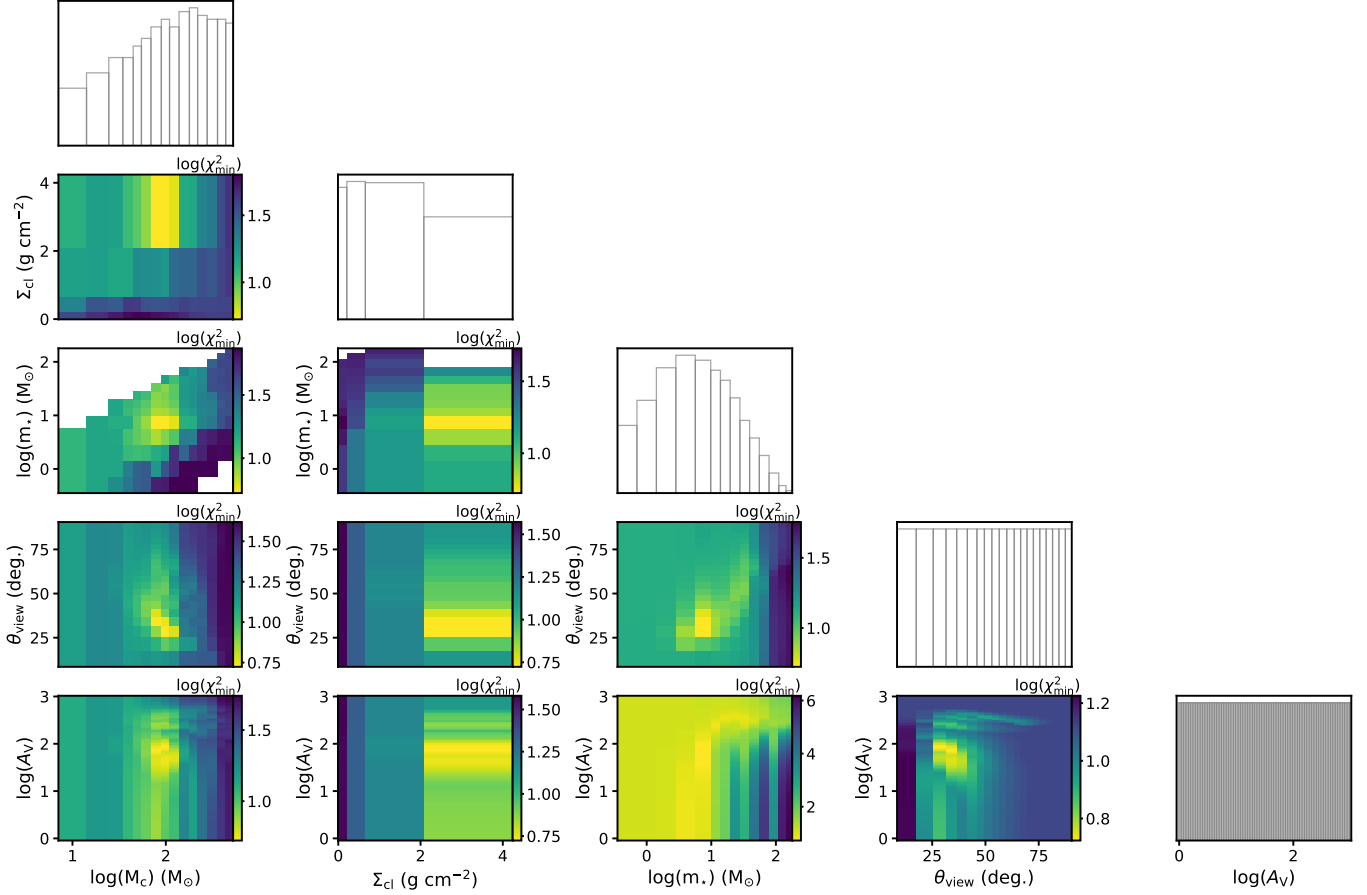


Figure 6. Distribution of the χ^2_{IMPRO} marginalized by model parameters. The IMPRO fitting uses all three bands, 37.1, 31.5, and 19.7 μm . The method and the legends are similar to those in Figure 5.

The drastic difference in the 1D profiles fitted by the SED and IMPRO methods comes from the fitted core properties. The SED model ($M_c = 120.0 M_\odot$; $\Sigma_{\text{cl}} = 0.316 \text{ g cm}^{-2}$; $M_* = 12.0 M_\odot$; $\theta_{\text{view}} = 51.0^\circ$ and $A_V = 70.5$) prefers a larger core ($R_c = 0.3 \text{ pc}$), while the 1D profile model ($M_c = 100.0 M_\odot$; $\Sigma_{\text{cl}} = 3.16 \text{ g cm}^{-2}$; $M_* = 8.0 M_\odot$; $\theta_{\text{view}} = 29.0^\circ$ and $A_V = 87.0$) converges on a smaller core ($R_c = 0.05 \text{ pc}$). Interestingly, the best-fitting IMPRO model fits the 1D profiles at 31.5 and 37.0 μm but underestimates the photometric fluxes at those bands on the SED. The 1D profile captures the brightness variation along the outflow axis, but ignores the shape of the outflow cavities, such as their opening angle. A larger opening angle would lead to a higher flux at mid-infrared wavelengths (e.g., Yang et al. 2017). Thus, the shape of outflow cavities may provide additional constraints for further improvements of the modeling.

We further compare the fitted model parameters with similar parameters derived from other observational studies. Introducing the 1D profile significantly improves the characterization of the θ_{view} to be $33.9^{+5.1}_{-4.9}^\circ$

(Table 1). Patel et al. (2005) derived an inclination angle of 62° for the disk using the aspect ratio of the dust and CH_3CN emission. Both the inclination of the disk and the θ_{view} of the outflow are defined with respect to the line of sight. Sanna et al. (2017) analyzed the kinematics of the CH_3OH maser spots and concluded that these maser spots have a preferential plane of motion, which inclines 64° from the plane of the sky. The residual inclination is $12^\circ \pm 9^\circ$. If the outflow is perpendicular to the disk midplane, the θ_{view} would be 28° and 26° for Patel et al. (2005) and Sanna et al. (2017). Our combined fitting method estimates the θ_{view} similar to that measured from disk inclination within its uncertainty.

The studies on the disk of Cep A also estimate the protostellar mass with dynamical analysis. Sanna et al. (2017) derived a mass of 5.5 and 10 M_\odot . The former reproduces the observed kinematics but only accounts for 10% of the observed L_{bol} , while the latter matches the L_{bol} but would indicate that magnetic fields reduce the observed maser velocities from the true Keplerian motion. Patel et al. (2005) estimated a binding mass

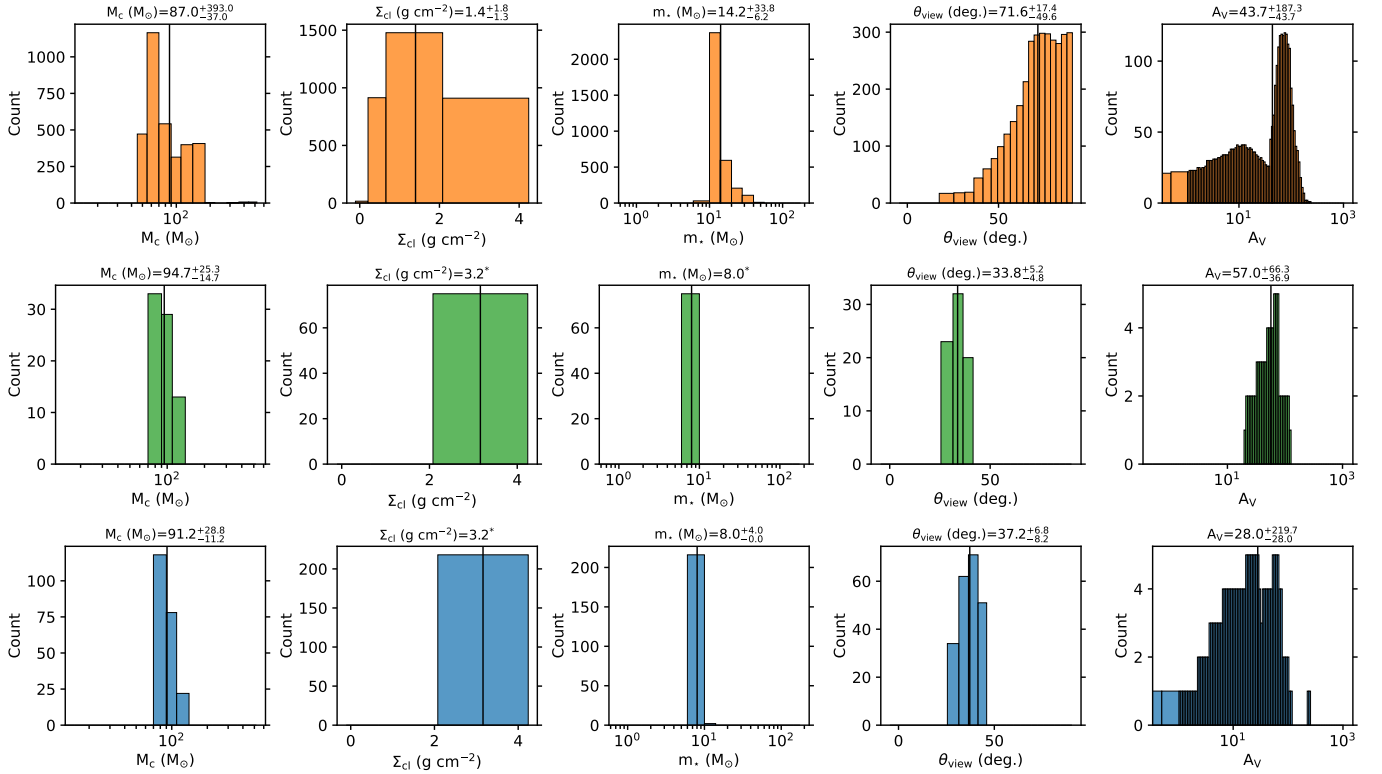


Figure 8. Distribution of the fitted parameters for the good models for Cep A. The good models are selected by $\chi^2_{\min} < \chi^2 < \chi^2_{\min} + 2$. The row shows the distribution of χ^2_{SED} , χ^2_{IMPRO} , and $\chi^2_{\text{SED+IMPRO}}$ from top to bottom. The mean value and the range of the model parameters are shown at the top of each panel. The minimum χ^2_{SED} , χ^2_{IMPRO} , and $\chi^2_{\text{SED+IMPRO}}$ are 0.69, 5.29, and 6.58, respectively. Note that the models with the minimum χ^2_{SED} and χ^2_{IMPRO} may not be the same model.

G35.20–0.74N (hereafter G35.2N; e.g., Gibb et al. 2003; Sánchez-Monge et al. 2013, 2014). The larger distance allows us to see how this fitting method performs with a worse physical resolution. Zhang et al. (2013b) presented a detailed modeling study using a similar theoretical framework as the one adopted here, where a single collapsing core could reproduce the SED and brightness profile along the outflow axis. The success of this modeling work makes G35.2N an important target to benchmark our combined modeling pipeline.

G35.2N is a massive star-forming region consisting of 17 compact continuum sources in sub-millimeter wavelengths arranged in a filament-like orientation (Sánchez-Monge et al. 2014; Beltrán et al. 2016; Zhang et al. 2022). Core A in Sánchez-Monge et al. (2014), Source 1 in Zhang et al. (2022), has the highest total sub-mm flux of the entire region, while Core B (Source 2) has the second highest sub-mm flux of $\sim 80\%$ of Core A; however, Core B is more compact than Core A, resulting in a higher peak continuum intensity. These two sources dominate the entire region and drive their own outflows. At sub-mm wavelengths, the outflows of Core A and B have position angles of $\sim 30^\circ$ and $\sim 6^\circ$, respectively. The outflows of Core A have a wide opening and ex-

tend to $40''$ – $60''$ (88,000–132,000 au; Birks et al. 2006), while the outflows of Core B are collimated and extend to $\sim 20''$ (Zhang et al. 2013b). Outflow signatures are also discovered in near-infrared, mm, and radio wavelengths (Gibb et al. 2003; Birks et al. 2006; Caratti o Garatti et al. 2015; Fedriani et al. 2019). The separation between Core A and B is only $\sim 2''$, which cannot be distinguished by the SOFIA observations. To determine the dominant source at infrared wavelengths, we rely on archival images from 3.6 to $37 \mu\text{m}$, showing that the outflow from Core B dominates the infrared emission (De Buizer 2006; Zhang et al. 2013b). Thus, for the fitting, we focus on Core B as the strip center. We also adopt the position angle of the outflow of Core B for the orientation of the strip.

We modeled the SED and the multi-band 1D profiles of G35.2N with the same prescription as that for Cep A. The only difference is the strip width. A nominal $20''$ width at the distance of G35.2N, 2.2 kpc (Zhang et al. 2009; Wu et al. 2014), corresponds to 44,000 au, which is larger than some synthetic images. More importantly, the strip width is chosen to best characterize the brightness profile along the outflow; therefore, the width for the G35.2N fitting should aim to have a similar physical

rebinned 1D profiles, essentially excluding the models with the core radii smaller than 7,700 au or 15,400 au. Figure 10 and 11 show the parameter distributions of the best models, chosen to have $\chi^2_{\min} \leq \chi^2 \leq \chi^2_{\min} + 2$. While the parameter distributions only change slightly for the SED fitting, the numbers of data points in the 1D profiles have a significant impact on the parameter distributions for the IMPRO fitting as well as the combined fitting. The distributions become a lot tighter when the minimum number of data points increases from 3 to 5, indicating a more robust prediction. However, the corresponding χ^2_{\min} becomes larger for the case with a minimum of 5 data points, suggesting that the fitting itself is becoming worse. Thus, increasing the minimum data points from 3 to 5 has no decisive improvement to the

Table 2. The best-fitting model parameters of G35.2N

Parameters	Fitting method		
	χ^2_{SED}	χ^2_{IMPRO}	$\chi^2_{\text{SED+IMPRO}}$
M_c (M_\odot)	$195.7^{+284.3}_{-135.7}$	$64.1^{+95.9}_{-24.1}$	$95.9^{+64.1}_{-45.9}$
Σ_{cl} (g cm^{-2})	$0.5^{+2.7}_{-0.4}$	$1.6^{+1.6}_{-0.6}$	$2.2^{+1.0}_{-1.2}$
m_* (M_\odot)	$17.1^{+30.9}_{-5.1}$	$14.7^{+49.3}_{-10.7}$	$13.1^{+50.9}_{-5.1}$
θ_{view} ($^\circ$)	$64.8^{+24.2}_{-42.8}$	$66.0^{+23.0}_{-53.0}$	$46.3^{+36.7}_{-24.3}$
A_V (mag)	$19.8^{+167.6}_{-19.8}$	$45.1^{+282.4}_{-45.1}$	$27.3^{+173.6}_{-27.3}$

NOTE: The uncertainties are taken from the full range of the distributions shown in Figure 10. The good models are selected from the models with a minimum of 3 data points in the 1D profiles.

fitting. For the following discussion on the fitting results of G35.2N, we focus on the fitting using a minimum of 3 data points in the 1D profiles. The mean values and their corresponding ranges are listed in Table 2.

The SED fitting and the 1D profile fitting produces different mean values of M_c by $\sim 130 M_\odot$ and both distributions shows an irregular shape with a gap, suggesting no obvious best-fitting value. By combining the SED and IMPRO fitting, the M_c distribution still lacks a single-peaked distribution. The Σ_{cl} from SED fitting has an primary peak at 0.316 g cm^{-2} with a broad distribution covering the entire sampling range ($0.1\text{--}3 \text{ g cm}^{-2}$) while the Σ_{cl} from IMPRO fitting peaks at 1.0 g cm^{-2} with 3.16 g cm^{-2} as the second best-fitting value. In the combined fitting, the Σ_{cl} of 1.0 g cm^{-2} is still the best-fitting value with 3.16 g cm^{-2} almost being equally good. For m_* , although the distribution changes modestly between the SED and IMPRO fitting, the combined fitting results in a multi-peaked distribution with a gap. However, the best-fitting m_* values are similar in different fitting methods. The distribution of θ_{view} changes between SED and IMPRO fitting, but the distribution remains relatively broad in IMPRO fitting in contrast to the substantially more narrow distribution found in the IMPRO fitting of Cep A. The distribution of θ_{view} in the combined fitting also has a gap, despite resulting in a consistent best-fitting value compared to that found in the SED and IMPRO fitting. For A_V , both SED and IMPRO fitting fail to constrain the value to a narrow range. In the combined fitting, the value of A_V , as expected from the lack of desired performance in the SED and IMPRO fitting, is not well constrained. In general, the improvement from the inclusion of 1D profile fitting is not apparent in the case of G35.2N, suggesting limitations in this fitting method in poorly-resolved sources (see Section 3.3).

For Core B, Sánchez-Monge et al. (2013) modeled the velocity structure of CH_3CN with Keplerian rotation

and estimated a central mass of $18 \pm 3 M_\odot$, which also includes a nearby continuum source separated by $0''.38$ (see also Beltrán et al. 2016). This companion source likely contributes little to the estimated mass because its dust mass is 20 times lower than that of Core B. Recently, in Core B, Zhang et al. (2022) modeled the free-free emission with a simple disk model and suggested a ZAMS stellar mass of 11.7 to $18.4 M_\odot$. They also discovered a spiral structure traced by SO_2 emission, indicative of instability of a massive disk. Our best-fitting values are mostly larger than those measurements, but consistent within the range of the good models. Due to the resolution of SOFIA, the model constrained by our combined fitting is likely to encompass the properties of both cores, yielding an effective protostellar core model. The m_* of $13.1 M_\odot$ is consistent with the mass of Core B and also consistent with the total mass of both cores, $22\text{--}30 M_\odot$, depending on the measurements of the protostellar mass of Core A (Sánchez-Monge et al. 2014). Zhang et al. (2013b) adopted a similar turbulent core model, where a clump is added and the outflows extend further outside the core radius, and found a m_* of $22\text{--}34 M_\odot$, higher than our best-fitting values and those derived from high-resolution observations.

Caratti o Garatti et al. (2015) derived A_V of 24 ± 4 mag and 12.5 ± 2.5 mag toward the center of Core A and the northeast end of the outflow associated with Core A. Their A_V estimates agree with the fitted A_V from our combined fitting; however, the good values have a much larger range compared to their uncertainties.

The rotating infalling envelope model constrained by the SO_2 emission suggests a disk inclination of 30° with respect to the line of sight (Zhang et al. 2022), corresponding to a θ_{view} of 60° if the outflow is perpendicular to the disk midplane. Our combined fitting suggests a θ_{view} of $46.3^{+36.7}_{-24.3}^\circ$. Despite the large uncertainty, our fitting estimates a θ_{view} consistent with that derived from high-resolution observations, while the SOFIA data used for the fitting do not resolve the disk.

3.3. Limitations of combined SED and IMPRO Fitting

As we demonstrated in the case of G35.2N (Section 3.2), combining IMPRO 1D intensity profile along the outflow axis fitting with SED fitting has little impact on improving constraints on ZT18 model grid parameters. On the other hand, in Cep A, after the inclusion of the 1D profiles, the parameter distributions of the good models substantially tighten. The main reason for the drastic difference in performance is likely the linear resolution of the observations. The distance of Cep A is 0.7 kpc , compared to 2.2 kpc for G35.2N. Thus, with SOFIA-FORCAST, the linear resolution for Cep A

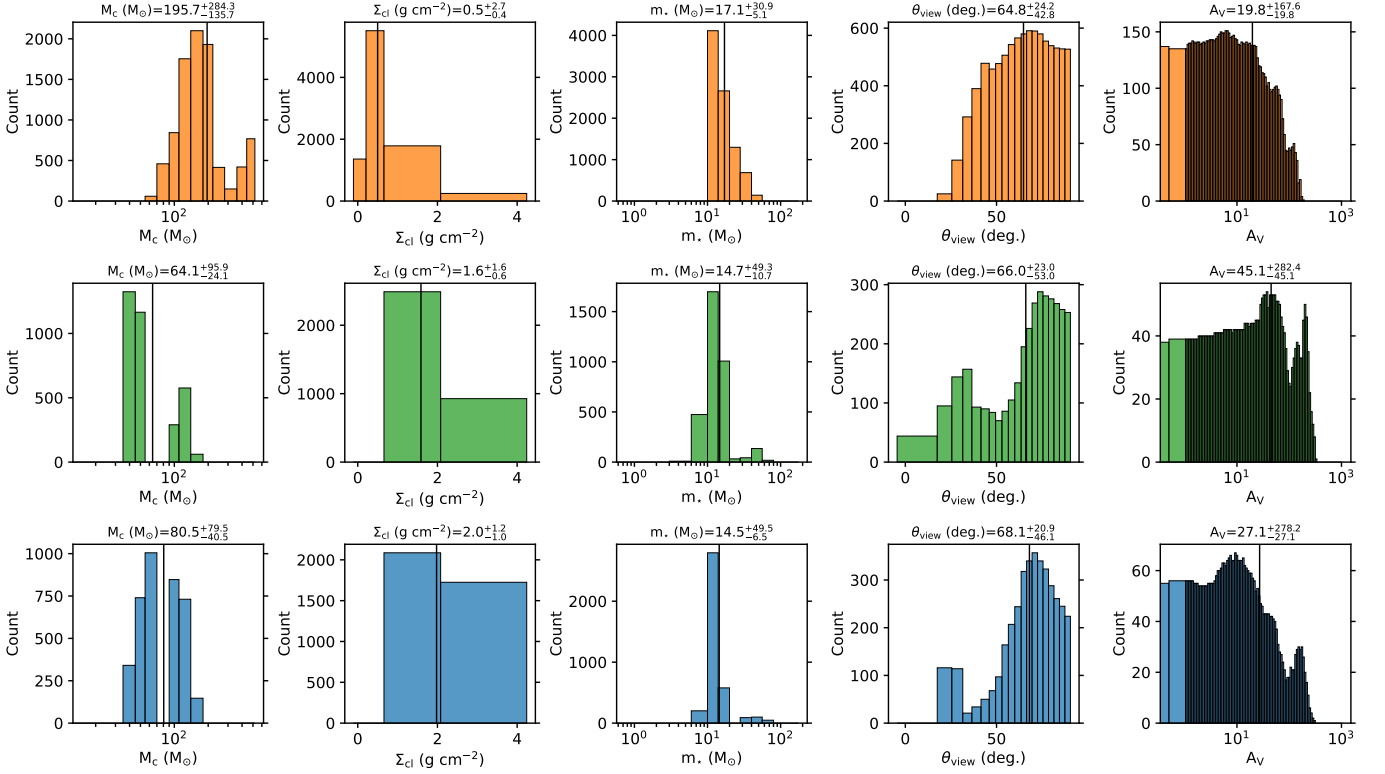


Figure 10. Distribution of the fitted parameters for the good models for G35.2N with at least 3 data points in any of its 1D profiles. We applied the same good model threshold (χ^2_{\min} to $\chi^2_{\min} + 2$). The figures are similar to those in Figure 8. The minimum χ^2_{SED} , χ^2_{IMPRO} , and $\chi^2_{\text{SED+IMPRO}}$ are 0.80, 4.44, and 5.76, respectively.

and G35.2N is ~ 2500 au and ~ 7700 au, respectively. As a result of the three times lower linear resolution for G35.2N, we needed to limit model testing for those with at least three data points in the 1D profiles. If the brightness profile along the outflow cannot be sufficiently resolved, adding the 1D profile to the SED fitting naturally has little effect. Figure 12 shows the distribution of the peak offsets in the 1D profiles for all the models in the ZT18 grid. A majority of the models have peak offsets $\lesssim 2000$ au, which is marginally resolved in the case of Cep A. At the distance of G35.2N, only a minor subset of models can be distinguished. Thus, while IMPRO fitting can provide unique constraints to the model parameters, observations with sufficient spatial resolution are required.

Intrinsic source properties may also affect the robustness of the profile modeling. Our modeling approach implicitly assumes a single protostar dominating the observed core, which has a symmetric outflow. However, massive star-forming regions can have multiple sources. G35.2N has at least four sources, each driving an outflow. While we focused on the likely dominant source for modeling, the presence of other sources may still contribute significantly to the observed brightness morphology and the SED. Furthermore, the bipolar outflow

may not be symmetric as assumed in the model. Asymmetry in outflow cavities and jets has been seen in multiple low-mass protostellar outflow (Habel et al. 2021; Hsieh et al. 2023). Such asymmetries can occur in high-mass outflows as well (e.g., Fedriani et al. 2023b; Crowe et al. 2025). Higher resolution observations will also help us better constrain these effects to revise the models of massive protostellar cores, as well as the fitting approach.

4. CONCLUSIONS

In this study, we developed an Image Profile (IMPRO) fitting method based on MIR/FIR intensity profiles along the outflow axis to constrain the fundamental properties of massive protostars. This IMPRO fitting has also been combined with SED fitting to yield the best joint constraints. In particular, for IMPRO fitting, we utilize the 1D intensity profile extracted from SOFIA-FORCAST images taken as part of the SOFIA Massive (SOMA) Star Formation survey at 19.7, 31.5, and 37.0 μm . Using Cep A as a test case, we found that the combined SED and IMPRO fitting approach results in more robust constraints on protostellar parameters in the ZT18 model grid. Particularly, the viewing angle (θ_{view}) becomes tightly constrained with the addition of

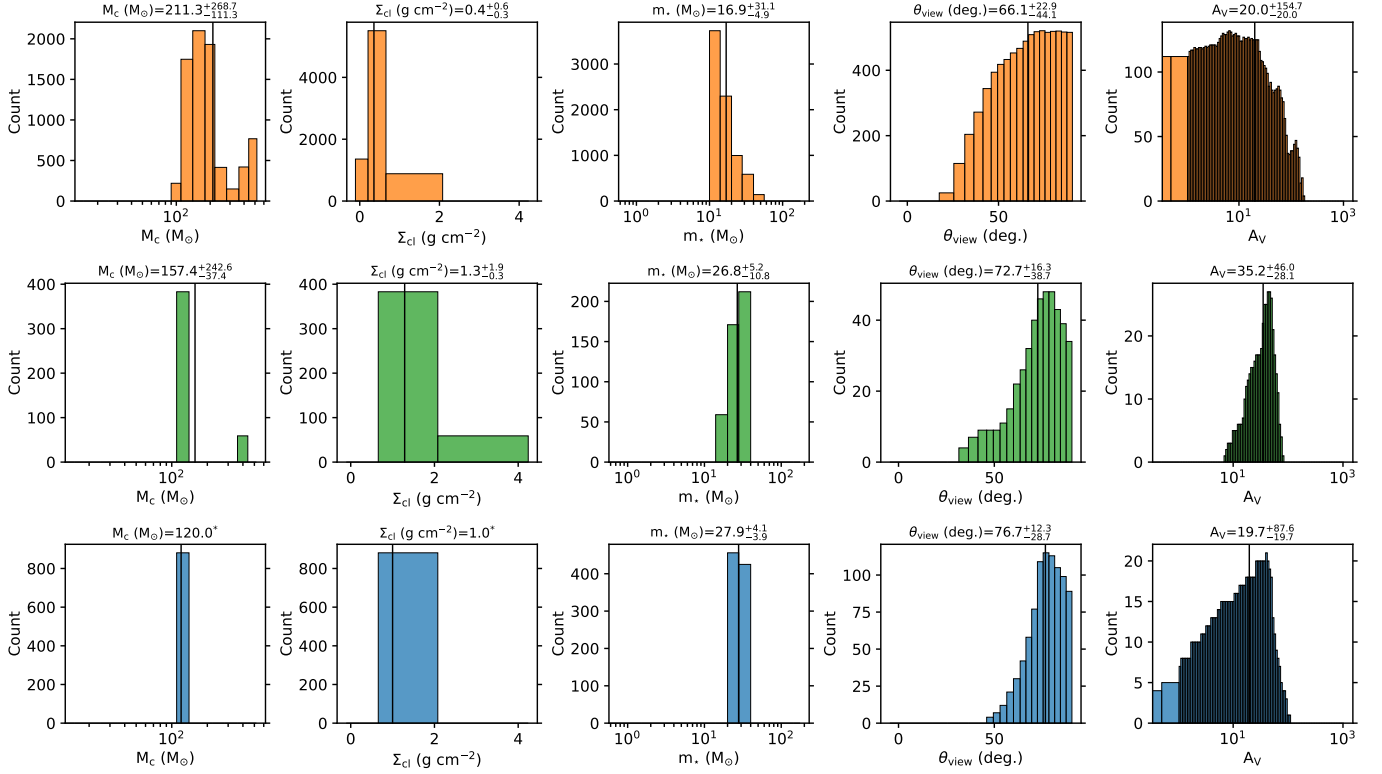


Figure 11. Distribution of the fitted parameters for the good models for G35.2N with at least 5 data points in any of its 1D profiles. These figures are similar to those in Figure 10. The minimum χ^2_{SED} , χ^2_{IMPRO} , and $\chi^2_{\text{SED+IMPRO}}$ are 0.80, 17.04, and 10.09, respectively. An asterisk indicates that all models have the same value.

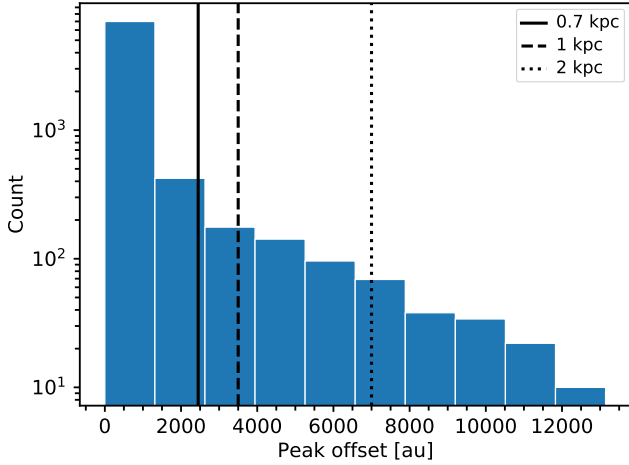


Figure 12. The distribution of the offsets of the peak brightness derived from the modeled images using a 20'' width strip. The solid, dashed, and dotted lines indicate the physical resolution of SOFIA at 37 μm at 0.7, 1.0, and 2.0 kpc.

the 1D intensity profiles. However, for G35.2N, a more distant source, this combined fitting method yields little improvement compared to the SED fitting alone due to the limited spatial resolution of the SOFIA-FORCAST observations. Thus, when fitting massive protostellar cores at distances ~ 2 kpc or greater, higher resolution

images are required to take advantage of the constraining power from the 1D profiles. We expect this fitting method to be applied to higher resolution infrared images taken by JWST NIRCам and MIRI.

Y.-L.Y. acknowledges the support from the Virginia Initiative of Cosmic Origins (VICO) Postdoctoral Fellowship. JCT acknowledges support from ERC Advanced Grant 788829 (MSTAR) and NSF grant AST-2206437. R.F. acknowledges support from the grants PID2023-146295NB-I00, and from the Severo Ochoa grant CEX2021-001131-S funded by MCIN/AEI/10.13039/501100011033 and by “European Union NextGenerationEU/PRTR”. Based on observations made with the NASA/DLR Stratospheric Observatory for Infrared Astronomy (SOFIA). SOFIA is jointly operated by the Universities Space Research Association, Inc. (USRA), under NASA contract NNA17BF53C, and the Deutsches SOFIA Institut (DSI) under DLR contract 50 OK 0901 to the University of Stuttgart. This research has made use of the NASA/IPAC Infrared Science Archive, which is funded by the National Aeronautics and Space Administration and operated by the California Institute of Technology.

Facilities: SOFIA

REFERENCES

- Beltrán, M. T., Cesaroni, R., Moscadelli, L., et al. 2016, *A&A*, 593, A49, doi: [10.1051/0004-6361/201628588](https://doi.org/10.1051/0004-6361/201628588)
- Beltrán, M. T., & de Wit, W. J. 2016, *A&A Rv*, 24, 6, doi: [10.1007/s00159-015-0089-z](https://doi.org/10.1007/s00159-015-0089-z)
- Beuther, H., Churchwell, E. B., McKee, C. F., & Tan, J. C. 2007, in *Protostars and Planets V*, ed. B. Reipurth, D. Jewitt, & K. Keil, 165, doi: [10.48550/arXiv.astro-ph/0602012](https://doi.org/10.48550/arXiv.astro-ph/0602012)
- Birks, J. R., Fuller, G. A., & Gibb, A. G. 2006, *A&A*, 458, 181, doi: [10.1051/0004-6361:20053209](https://doi.org/10.1051/0004-6361:20053209)
- Bonnell, I. A., Bate, M. R., Clarke, C. J., & Pringle, J. E. 2001, *MNRAS*, 323, 785, doi: [10.1046/j.1365-8711.2001.04270.x](https://doi.org/10.1046/j.1365-8711.2001.04270.x)
- Brogan, C. L., Chandler, C. J., Hunter, T. R., Shirley, Y. L., & Sarma, A. P. 2007, *ApJL*, 660, L133, doi: [10.1086/518390](https://doi.org/10.1086/518390)
- Caratti o Garatti, A., Stecklum, B., Linz, H., Garcia Lopez, R., & Sanna, A. 2015, *A&A*, 573, A82, doi: [10.1051/0004-6361/201423992](https://doi.org/10.1051/0004-6361/201423992)
- Carrasco-González, C., Sanna, A., Rodríguez-Kamenetzky, A., et al. 2021, *ApJL*, 914, L1, doi: [10.3847/2041-8213/abf735](https://doi.org/10.3847/2041-8213/abf735)
- Crowe, S., Fedriani, R., Tan, J. C., et al. 2025, *ApJ*, 983, 19, doi: [10.3847/1538-4357/ad8889](https://doi.org/10.3847/1538-4357/ad8889)
- Cunningham, N. J., Moeckel, N., & Bally, J. 2009, *The Astrophysical Journal*, 692, 943, doi: [10.1088/0004-637X/692/2/943](https://doi.org/10.1088/0004-637X/692/2/943)
- Cunningham, N. J., Moeckel, N., & Bally, J. 2009, *ApJ*, 692, 943, doi: [10.1088/0004-637X/692/2/943](https://doi.org/10.1088/0004-637X/692/2/943)
- Curiel, S., Ho, P. T. P., Patel, N. A., et al. 2006, *ApJ*, 638, 878, doi: [10.1086/498931](https://doi.org/10.1086/498931)
- De Buizer, J. M. 2006, *ApJL*, 642, L57, doi: [10.1086/504291](https://doi.org/10.1086/504291)
- De Buizer, J. M., Liu, M., Tan, J. C., et al. 2017, *ApJ*, 843, 33, doi: [10.3847/1538-4357/aa74c8](https://doi.org/10.3847/1538-4357/aa74c8)
- Durjasz, M., Szymczak, M., Olech, M., & Bartkiewicz, A. 2022, *A&A*, 663, A123, doi: [10.1051/0004-6361/202243552](https://doi.org/10.1051/0004-6361/202243552)
- Evans, II, N. J., Becklin, E. E., Beichman, C., et al. 1981, *ApJ*, 244, 115, doi: [10.1086/158690](https://doi.org/10.1086/158690)
- Fedriani, R., Caratti o Garatti, A., Purser, S. J. D., et al. 2019, *Nature Communications*, 10, 3630, doi: [10.1038/s41467-019-11595-x](https://doi.org/10.1038/s41467-019-11595-x)
- Fedriani, R., Tan, J. C., Telkamp, Z., et al. 2023a, *ApJ*, 942, 7, doi: [10.3847/1538-4357/aca4cf](https://doi.org/10.3847/1538-4357/aca4cf)
- Fedriani, R., Caratti o Garatti, A., Cesaroni, R., et al. 2023b, *A&A*, 676, A107, doi: [10.1051/0004-6361/202346736](https://doi.org/10.1051/0004-6361/202346736)
- Frost, A. J., Oudmaijer, R. D., de Wit, W. J., & Lumsden, S. L. 2019, *A&A*, 625, A44, doi: [10.1051/0004-6361/201834583](https://doi.org/10.1051/0004-6361/201834583)
- . 2021a, *A&A*, 648, A62, doi: [10.1051/0004-6361/202039748](https://doi.org/10.1051/0004-6361/202039748)
- Frost, A. J., Oudmaijer, R. D., Lumsden, S. L., & de Wit, W. J. 2021b, *ApJ*, 920, 48, doi: [10.3847/1538-4357/ac1741](https://doi.org/10.3847/1538-4357/ac1741)
- Garay, G., Ramirez, S., Rodriguez, L. F., Curiel, S., & Torrelles, J. M. 1996, *ApJ*, 459, 193, doi: [10.1086/176882](https://doi.org/10.1086/176882)
- Gibb, A. G., Hoare, M. G., Little, L. T., & Wright, M. C. H. 2003, *MNRAS*, 339, 1011, doi: [10.1046/j.1365-8711.2003.06251.x](https://doi.org/10.1046/j.1365-8711.2003.06251.x)
- Gómez, J. F., Sargent, A. I., Torrelles, J. M., et al. 1999, *ApJ*, 514, 287, doi: [10.1086/306916](https://doi.org/10.1086/306916)
- Green, J. D., Watson, D. M., Bergin, E., et al. 2011, *ApJL*, 726, L1, doi: [10.1088/2041-8205/726/1/L1](https://doi.org/10.1088/2041-8205/726/1/L1)
- Gyulbudaghian, A. L., Glushkov, Y. I., & Denisyuk, E. K. 1978, *ApJL*, 224, L137, doi: [10.1086/182777](https://doi.org/10.1086/182777)
- Habel, N. M., Megeath, S. T., Booker, J. J., et al. 2021, *ApJ*, 911, 153, doi: [10.3847/1538-4357/abded8](https://doi.org/10.3847/1538-4357/abded8)
- Hartigan, P., Lada, C. J., Stocke, J., & Tapia, S. 1986, *AJ*, 92, 1155, doi: [10.1086/114247](https://doi.org/10.1086/114247)
- Hartigan, P., Morse, J., & Bally, J. 2000, *AJ*, 120, 1436, doi: [10.1086/301522](https://doi.org/10.1086/301522)
- Hsieh, C.-H., Arce, H. G., Li, Z.-Y., et al. 2023, *ApJ*, 947, 25, doi: [10.3847/1538-4357/acba13](https://doi.org/10.3847/1538-4357/acba13)
- Hughes, V. A., & Wouterloot, J. G. A. 1984, *ApJ*, 276, 204, doi: [10.1086/161603](https://doi.org/10.1086/161603)
- Kim, S.-H., Martin, P. G., & Hendry, P. D. 1994, *ApJ*, 422, 164, doi: [10.1086/173714](https://doi.org/10.1086/173714)
- Liu, M., Tan, J. C., De Buizer, J. M., et al. 2019, *ApJ*, 874, 16, doi: [10.3847/1538-4357/ab07b7](https://doi.org/10.3847/1538-4357/ab07b7)
- . 2020, *ApJ*, 904, 75, doi: [10.3847/1538-4357/abbefb](https://doi.org/10.3847/1538-4357/abbefb)
- McKee, C. F., & Tan, J. C. 2003, *ApJ*, 585, 850, doi: [10.1086/346149](https://doi.org/10.1086/346149)
- Miotello, A., Kamp, I., Birnstiel, T., Cleeves, L. C., & Kataoka, A. 2023, in *Astronomical Society of the Pacific Conference Series*, Vol. 534, *Protostars and Planets VII*, ed. S. Inutsuka, Y. Aikawa, T. Muto, K. Tomida, & M. Tamura, 501, doi: [10.48550/arXiv.2203.09818](https://doi.org/10.48550/arXiv.2203.09818)
- Moriarty-Schieven, G. H., Snell, R. L., & Hughes, V. A. 1991, *ApJ*, 374, 169, doi: [10.1086/170106](https://doi.org/10.1086/170106)

- Moscadelli, L., Reid, M. J., Menten, K. M., et al. 2009, *ApJ*, 693, 406, doi: [10.1088/0004-637X/693/1/406](https://doi.org/10.1088/0004-637X/693/1/406)
- Patel, N. A., Curiel, S., Sridharan, T. K., et al. 2005, *Nature*, 437, 109, doi: [10.1038/nature04011](https://doi.org/10.1038/nature04011)
- Reipurth, B., & Raga, A. C. 1999, in *NATO Advanced Study Institute (ASI) Series C*, Vol. 540, *The Origin of Stars and Planetary Systems*, ed. C. J. Lada & N. D. Kylafis, 267
- Rodriguez, L. F., Ho, P. T. P., & Moran, J. M. 1980, *ApJL*, 240, L149, doi: [10.1086/183342](https://doi.org/10.1086/183342)
- Rosero, V., Tanaka, K. E. I., Tan, J. C., et al. 2019, *ApJ*, 873, 20, doi: [10.3847/1538-4357/ab0209](https://doi.org/10.3847/1538-4357/ab0209)
- Sánchez-Monge, Á., Cesaroni, R., Beltrán, M. T., et al. 2013, *A&A*, 552, L10, doi: [10.1051/0004-6361/201321134](https://doi.org/10.1051/0004-6361/201321134)
- Sánchez-Monge, Á., Beltrán, M. T., Cesaroni, R., et al. 2014, *A&A*, 569, A11, doi: [10.1051/0004-6361/201424032](https://doi.org/10.1051/0004-6361/201424032)
- Sanna, A., Moscadelli, L., Surcis, G., et al. 2017, *A&A*, 603, A94, doi: [10.1051/0004-6361/201730773](https://doi.org/10.1051/0004-6361/201730773)
- Sanna, A., Oliva, A., Moscadelli, L., et al. 2025, arXiv e-prints, arXiv:2502.15070, doi: [10.48550/arXiv.2502.15070](https://doi.org/10.48550/arXiv.2502.15070)
- Sugiyama, K., Fujisawa, K., Doi, A., et al. 2008, *PASJ*, 60, 1001, doi: [10.1093/pasj/60.5.1001](https://doi.org/10.1093/pasj/60.5.1001)
- Tan, J. C., Beltrán, M. T., Caselli, P., et al. 2014, in *Protostars and Planets VI*, ed. H. Beuther, R. S. Klessen, C. P. Dullemond, & T. Henning, 149–172, doi: [10.2458/azu_uapress_9780816531240-ch007](https://doi.org/10.2458/azu_uapress_9780816531240-ch007)
- Telkamp, Z., Fedriani, R., Tan, J. C., et al. 2025, *ApJ*, 986, 15, doi: [10.3847/1538-4357/adcd79](https://doi.org/10.3847/1538-4357/adcd79)
- Torrelles, J. M., Patel, N. A., Curiel, S., et al. 2007, *ApJL*, 666, L37, doi: [10.1086/521675](https://doi.org/10.1086/521675)
- Torrelles, J. M., Rodriguez, L. F., Canto, J., & Ho, P. T. P. 1993, *ApJL*, 404, L75, doi: [10.1086/186747](https://doi.org/10.1086/186747)
- Torrelles, J. M., Patel, N. A., Curiel, S., et al. 2011, *MNRAS*, 410, 627, doi: [10.1111/j.1365-2966.2010.17483.x](https://doi.org/10.1111/j.1365-2966.2010.17483.x)
- Wu, Y. W., Sato, M., Reid, M. J., et al. 2014, *A&A*, 566, A17, doi: [10.1051/0004-6361/201322765](https://doi.org/10.1051/0004-6361/201322765)
- Yang, Y.-L., Evans, II, N. J., Green, J. D., Dunham, M. M., & Jørgensen, J. K. 2017, *ApJ*, 835, 259, doi: [10.3847/1538-4357/835/2/259](https://doi.org/10.3847/1538-4357/835/2/259)
- Zapata, L. A., Fernandez-Lopez, M., Curiel, S., Patel, N., & Rodriguez, L. F. 2013, arXiv e-prints, arXiv:1305.4084, doi: [10.48550/arXiv.1305.4084](https://doi.org/10.48550/arXiv.1305.4084)
- Zhang, B., Zheng, X. W., Reid, M. J., et al. 2009, *ApJ*, 693, 419, doi: [10.1088/0004-637X/693/1/419](https://doi.org/10.1088/0004-637X/693/1/419)
- Zhang, Y., & Tan, J. C. 2011, *ApJ*, 733, 55, doi: [10.1088/0004-637X/733/1/55](https://doi.org/10.1088/0004-637X/733/1/55)
- . 2018, *ApJ*, 853, 18, doi: [10.3847/1538-4357/aaa24a](https://doi.org/10.3847/1538-4357/aaa24a)
- Zhang, Y., Tan, J. C., & Hosokawa, T. 2014, *ApJ*, 788, 166, doi: [10.1088/0004-637X/788/2/166](https://doi.org/10.1088/0004-637X/788/2/166)
- Zhang, Y., Tan, J. C., & McKee, C. F. 2013a, *ApJ*, 766, 86, doi: [10.1088/0004-637X/766/2/86](https://doi.org/10.1088/0004-637X/766/2/86)
- Zhang, Y., Tan, J. C., De Buizer, J. M., et al. 2013b, *ApJ*, 767, 58, doi: [10.1088/0004-637X/767/1/58](https://doi.org/10.1088/0004-637X/767/1/58)
- Zhang, Y., Tanaka, K. E. I., Tan, J. C., et al. 2022, *ApJ*, 936, 68, doi: [10.3847/1538-4357/ac847f](https://doi.org/10.3847/1538-4357/ac847f)